High-yield production of graphene by liquid-phase exfoliation of graphite

YENNY HERNANDEZ[1†], VALERIA NICOLOSI[1†], MUSTAFA LOTYA[1], FIONA M. BLIGHE[1], ZHENYU SUN[1,2], SUKANTA DE[1,2], I. T. McGOVERN[1], BRENDAN HOLLAND[1], MICHELE BYRNE[3], YURII K. GUN'KO[2,3], JOHN J. BOLAND[2,3], PETER NIRAJ[2,3], GEORG DUESBERG[2,3], SATHEESH KRISHNAMURTHY[2,3], ROBBIE GOODHUE[4], JOHN HUTCHISON[5], VITTORIO SCARDACI[6], ANDREA C. FERRARI[6] AND JONATHAN N. COLEMAN[1,2]*

[1]School of Physics, Trinity College Dublin, Dublin 2, Ireland
[2]Centre for Research on Adaptive Nanostructures and Nanodevices (CRANN), Trinity College Dublin, Dublin 2, Ireland
[3]School of Chemistry, Trinity College Dublin, Dublin 2, Ireland
[4]Department of Geology, School of Natural Sciences, Trinity College Dublin, Dublin 2, Ireland
[5]Department of Materials, University of Oxford, Parks Road, Oxford OX1 3PH, UK
[6]Engineering Department, University of Cambridge, 9 JJ Thomson Avenue, Cambridge CB3 0FA, UK
†These authors contributed equally to this work.
*e-mail: colemaj@tcd.ie

Fully exploiting the properties of graphene will require a method for the mass production of this remarkable material. Two main routes are possible: large-scale growth or large-scale exfoliation. Here, we demonstrate graphene dispersions with concentrations up to ∼0.01 mg ml^{-1}, produced by dispersion and exfoliation of graphite in organic solvents such as N-methyl-pyrrolidone. This is possible because the energy required to exfoliate graphene is balanced by the solvent–graphene interaction for solvents whose surface energies match that of graphene. We confirm the presence of individual graphene sheets by Raman spectroscopy, transmission electron microscopy and electron diffraction. Our method results in a monolayer yield of ∼1 wt%, which could potentially be improved to 7–12 wt% with further processing. The absence of defects or oxides is confirmed by X-ray photoelectron, infrared and Raman spectroscopies. We are able to produce semi-transparent conducting films and conducting composites. Solution processing of graphene opens up a range of potential large-area applications, from device and sensor fabrication to liquid-phase chemistry.

The novel electronic properties of graphene have been well documented[1]; the charge carriers behave as massless Dirac fermions[2], and novel effects such as an ambipolar field effect[3], a room-temperature quantum Hall effect[4] and the breakdown of the Born–Oppenheimer approximation[5] have all been observed. A graphene monolayer has also been demonstrated as a transparent electrode in a liquid crystal device[6]. However, as was the case in the early days of nanotube and nanowire research, graphene suffers from a problem that is common to many novel materials — the lack of a method for producing it at high yields. The standard procedure used to make graphene is micromechanical cleavage[7]. This gives the best samples to date, with carrier mobilities up to 200,000 cm^2 V^{-1} s^{-1} (refs 8–10). However, the single layers so obtained form a negligible fraction amongst large quantities of thin graphite flakes. Furthermore, it is difficult to envisage how to scale up this process to mass production. Alternatively, growth of graphene is also commonly achieved by annealing SiC substrates; however, these samples are in fact composed of a multitude of domains, most of them submicrometre in scale, and they are not spatially uniform in number or size over larger length scales[11–13]. A number of works have also reported graphene growth on metal substrates[14–17], but this would require transfer of the sample to insulating substrates

in order to make useful devices, either by mechanical transfer or through solution processing.

Recently, a large number of papers have described the dispersion and exfoliation of graphene oxide (GO)[18–21]. This material consists of graphene-like sheets, chemically functionalized with compounds such as hydroxyls and epoxides, which stabilize the sheets in water[22]. However, this functionalization disrupts the electronic structure of graphene. In fact GO is an insulator[23] rather than a semi-metal and is conceptually different from graphene. Although the functional groups can be removed by reduction, so far this leaves a significant number of defects, which continue to disrupt the electronic properties, remain[18,22]. Thus, a non-covalent, solution-phase method to produce significant quantities of defect-free, unoxidized graphene is urgently required. In this paper we propose one such method.

Here we show that high-quality monolayer graphene can be produced at significant yields by non-chemical, solution-phase exfoliation of graphite in certain organic solvents. This work builds upon over 50 years of study into chemical exfoliation of graphite[24]. Previously, intercalated graphite could be partially exfoliated by reactions involving the intercalant[25], through thermal shock[26] or by acid treatment of expandable graphite[27]. However, to date, such methods have given thin graphite sheets or graphene

fragments[27] rather than large-scale graphene monolayers. The response to this problem has so far been the exfoliation of chemically modified forms of graphene such as GO or functionalized graphene[20,22,28]. However, such materials are not graphene, as they are insulators containing numerous structural defects[22,28] that cannot, so far, be fully removed by chemical treatment[22]. Our method results in high-quality, unoxidized monolayer graphene at yields of ~1 wt%. We show that the process could potentially be improved to give yields of up to 12 wt% of the starting graphite mass with sediment recycling. As a solution-phase method it is versatile, it may be scaled up, and it can be used to deposit graphene in a variety of environments and substrates not available using cleavage or growth methods. Furthermore, it can be used to produce graphene-based composites or films, a key requirement for many applications, such as thin-film transistors, conductive transparent electrodes for indium tin oxide replacement or for photovoltaics.

DISPERSION OF GRAPHITE

Recently, carbon nanotubes have been successfully exfoliated in a small number of solvents such N-methylpyrrolidone (NMP)[29–33]. Such exfoliation occurs because the strong interaction between solvent and nanotube sidewall means that the energetic penalty for exfoliation and subsequent solvation becomes small[34]. We suggest that similar effects may occur between these solvents and graphene. To test this we prepared a dispersion of sieved graphite powder (Aldrich product 332461, batch number 06106DE) in NMP (spectrophotometric grade, >99.0%) by bath sonication (see Supplementary Information, Section S1.2). After sonication we obtained a grey liquid consisting of a homogeneous phase and large numbers of macroscopic aggregates. As with nanotube dispersions[30,32], these aggregates could be removed by mild centrifugation, giving a homogeneous dark dispersion. Such dispersions, prepared at different graphite concentrations, are shown in Fig. 1a. Although moderate levels of sedimentation and aggregation occur within three weeks of centrifugation, the dispersions remain of high quality at least five months after preparation (see Supplementary Information, Section S2.4).

In order to find the concentration after centrifugation, we passed the graphite dispersion through polyvinylidene fluoride (PVDF) filters. Careful measurements of the filtered mass, accounting for residual solvent, gave the concentration of dispersed phase after centrifugation. This procedure was repeated for three other solvents known to successfully disperse nanotubes[34]: N,N-Dimethylacetamide (DMA), γ-butyrolactone (GBL) and 1,3-dimethyl-2-imidazolidinone (DMEU). These dispersions were then characterized by UV–vis–IR absorption spectroscopy, with the absorption coefficient plotted versus wavelength (Fig. 1b). The spectra are featureless in the visible–IR region as expected[35]. Each of these four dispersions was diluted a number of times and the absorption spectra recorded. The absorbance (660 nm) divided by cell length is plotted versus concentration (Fig. 1c), showing Lambert–Beer behaviour for all solvents, $\langle \alpha_{660} \rangle = 2{,}460$ L g^{-1} m^{-1}.

Thus, it is clear that graphite can be dispersed in some solvents. As we will show, the graphite is almost completely exfoliated to multilayer structures with <5 layers in NMP, GBL and DMEU, if not other solvents. In addition, significant quantities of individual monolayers are also present. The question is what solvent properties lead to this exfoliation of graphite?

Such exfoliation can only occur if the net energetic cost is very small. In chemistry, this energy balance is expressed as the enthalpy of mixing (per unit volume), which we can
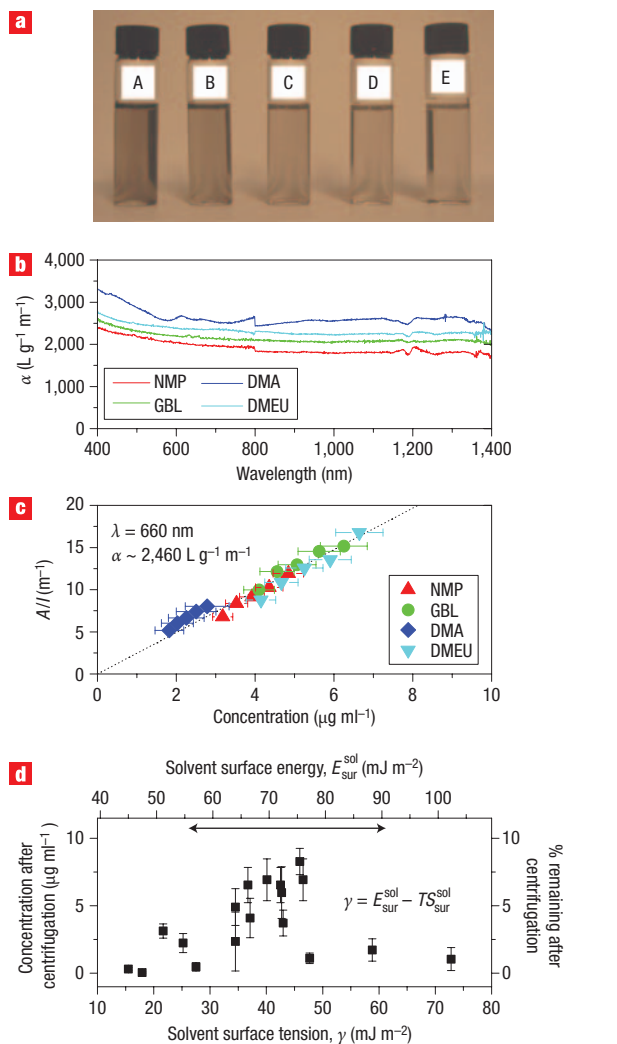
Figure 1 Optical characterization of graphite dispersions. a, Dispersions of graphite flakes in NMP, at a range of concentrations ranging from 6 μg ml^{-1} (A) to 4 μg ml^{-1} (E) after centrifugation. **b**, Absorption spectra for graphite flakes dispersed in NMP, GBL, DMA and DMEU at concentrations from 2 to 8 μg ml^{-1}. **c**, Optical absorbance ($\lambda_{ex} = 660$ nm) divided by cell length (A/l) as a function of concentration for graphene in the four solvents NMP, GBL, DMA and DMEU showing Lambert–Beer behaviour with an average absorption coefficient of $\langle \alpha_{660} \rangle = 2{,}460$ L g^{-1} m^{-1}. The x-axis error bars come from the uncertainty in measuring the mass of graphene/graphite in solution. **d**, Graphite concentration measured after centrifugation for a range of solvents plotted versus solvent surface tension. The data were converted from absorbance (660 nm) using $A/l = \langle \alpha_{660} \rangle C$ with $\langle \alpha_{660} \rangle = 2{,}460$ L g^{-1} m^{-1}. The original concentration, before centrifugation, was 0.1 mg ml^{-1}. The y-axis error bars represent the standard deviation calculated from five measurements. Shown on the right axis is the percentage of material remaining after centrifugation. On the top axis, the surface tension has been transformed into surface energy using a universal value for surface entropy of $S_{sur}^{sol} \approx 0.1$ mJ K^{-1} m^{-2}. The horizontal arrow shows the approximate range of the reported literature values for the surface energy of graphite[39–42].

approximately calculate in this case to be (see Supplementary Information, Section S6.0):

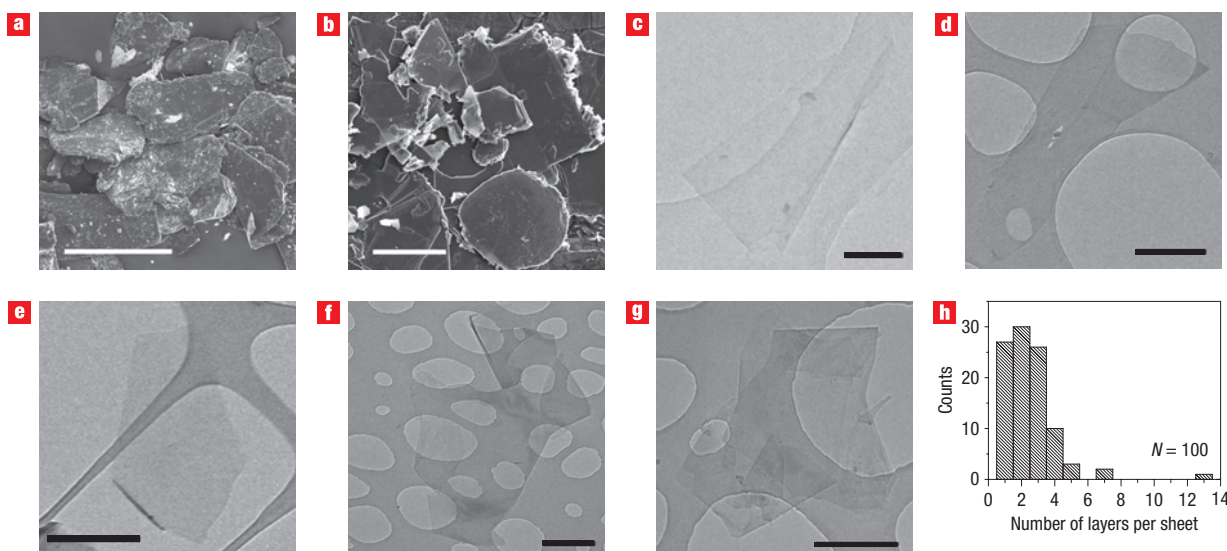$$\frac{\Delta H_{mix}}{V_{mix}} \approx \frac{2}{T_{flake}} (\delta_G - \delta_{sol})^2 \phi \qquad (1)$$

Figure 2 Electron microscopy of graphite and graphene. a, SEM image of sieved, pristine graphite (scale bar: 500 μm). **b,** SEM image of sediment after centrifugation (scale bar: 25 μm). **c−e,** Bright-field TEM images of monolayer graphene flakes deposited from GBL (**c**), DMEU (**d**) and NMP (**e**), respectively (scale bars: 500 nm). **f,g,** Bright-field TEM images of a folded graphene sheet and multilayer graphene, both deposited from NMP (scale bars: 500 nm). **h,** Histogram of the number of visual observations of flakes as a function of the number of monolayers per flake for NMP dispersions.

where $\delta_i = \sqrt{(E_{sur}^i)}$ is the square root of the surface energy of phase i, T_{flake} is the thickness of a graphene flake and ϕ is the graphene volume fraction. Reminiscent of the Hildebrand−Scratchard equation[36], this shows the enthalpy of mixing is dependent on the balance of graphene and solvent surface energies. For graphite, the surface energy is defined as the energy per unit area required to overcome the van der Waals forces when peeling two sheets apart.

From equation (1), we expect a minimal energy cost of exfoliation for solvents whose surface energy matches that of graphene. To test this, we dispersed graphite in a wide range of solvents. By measuring the optical absorbance after mild centrifugation and using the absorption coefficient (660 nm) to transform absorbance into concentration, we can quantify the amount of graphite flakes dispersed as a function of solvent surface energy (calculated from surface tension[37,38], see Fig. 1 caption) as shown in Fig. 1d. As predicted, the dispersed concentration shows a strong peak for solvents with a surface energy very close to the literature values of the nanotube/graphite surface energy[39–42] (that is, $\sim 70-80$ mJ m^{-2}). Coupled with equation (1), this strongly suggests that not only is the enthalpy of mixing for graphite dispersed in good solvents very close to zero, but the solvent−graphite interaction is van der Waals rather than covalent. In addition, it predicts that good solvents are characterized by surface tensions in the region of $40-50$ mJ m^{-2}. Also, we can tell from these data that for the best solvent (benzyl benzoate), 8.3% by mass of the original material remained after centrifugation. (For NMP, 7.6% remained.)

It is crucial to ascertain the exfoliation state of the material that remains dispersed after centrifugation. First we examined the state of the initial graphite powder. Scanning electron microscopy (SEM) studies (Fig. 2a) show the starting powder to consist of flakes of lateral size <500 μm and thickness <100 μm. In comparison, the sediment separated after centrifugation contains flakes, which are much smaller, with lateral size measured in tens of micrometres with thicknesses of a few micrometres (Fig. 2b). Clearly, sonication results in fragmentation of the initial flakes, with the largest removed by centrifugation. We note that, as the

crystallite size in the starting powder was >150 μm, the preparation procedure must result in tearing of the crystallites. This process may be similar to sonication-induced fragmentation of carbon nanotubes[43].

EVIDENCE OF EXFOLIATION TO GRAPHENE

It is possible to investigate the state of the material remaining dispersed using transmission electron microscopy (TEM) by dropping a small quantity of each dispersion onto holey carbon grids. Crucially, this technique is simpler than that previously used to prepare graphene for TEM[44], which involved under-etching of graphene placed on a silicon substrate. Immediately apparent in the present technique is the advantage of having graphite dispersions. Figure 2c−g shows bright-field TEM images of the objects typically observed, which generally fall into three classes. The first class, as shown in Fig. 2c−e, comprises monolayer graphene. Second, in a number of cases we observe folded graphene layers (Fig. 2f). Third, we find bilayer and multilayer graphene (Fig. 2g). In all cases, these objects have lateral sizes typically of a few micrometres. In some cases the sheet edges tend to scroll and fold slightly (see Supplementary Information, Fig. S3b). However, we rarely observe large objects with thickness of more than a few layers. Thus we believe that, in these samples, graphite has been extensively exfoliated to give monolayer and few-layer graphene. By analysing a large number of TEM images, paying close attention to the uniformity of the flake edges, we can generate flake thickness statistics as shown in Fig. 2h. From these data we can estimate the number fraction of monolayer graphene (number of monolayers/total number of flakes observed) in NMP dispersions as 28%. This corresponds to a solution-phase monolayer mass fraction (mass of all monolayers/mass of all flakes observed) of ~ 12 wt%, leading to an overall yield (mass of monolayers/starting graphite mass) of ~ 1 wt% (see Supplementary Information, Table S2 and Section S2.3). In fact, we also find that the sediment can be recycled to produce dispersions with number and mass fractions of
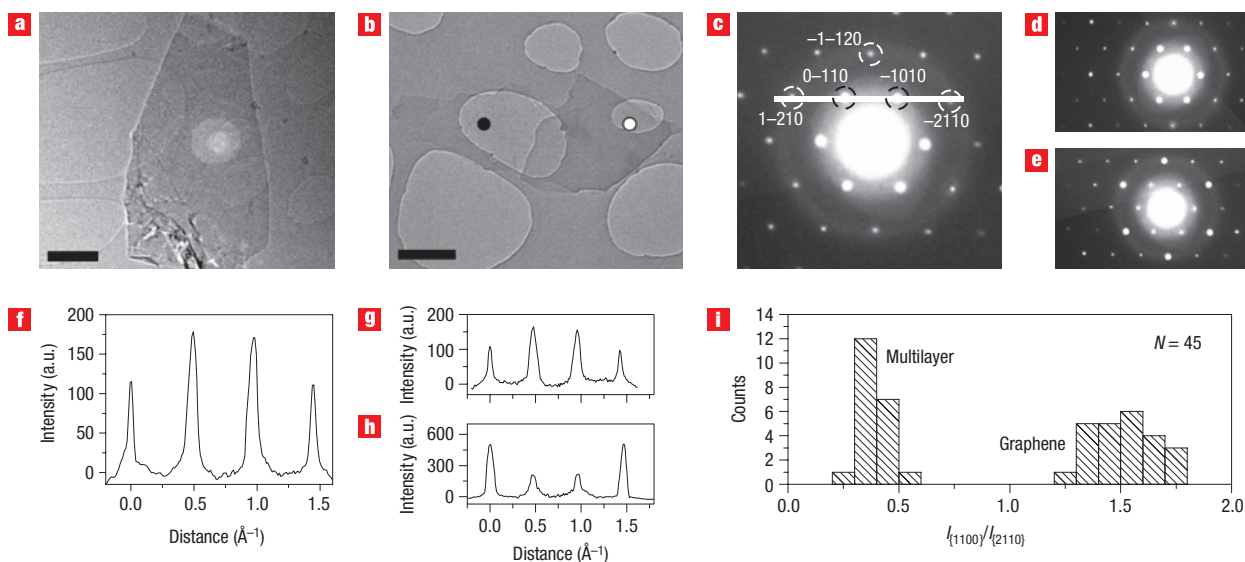
Figure 3 Evidence of monolayer graphene from TEM. a,b, High-resolution TEM images of solution-cast monolayer (**a**) and bilayer (**b**) graphene (scale bar 500 nm). **c**, Electron diffraction pattern of the sheet in **a**, with the peaks labelled by Miller−Bravais indices. **d,e**, Electron diffraction patterns taken from the positions of the black (**d**) and white spots (**e**), respectively, of the sheet shown in **b**, using the same labels as in **c**. The graphene is clearly one layer thick in **d** and two layers thick in **e**. **f−h**, Diffracted intensity taken along the 1−210 to −2110 axis for the patterns shown in **c−e**, respectively. **i**, Histogram of the ratios of the intensity of the {1100} and {2110} diffraction peaks for all the diffraction patterns collected. A ratio >1 is a signature of graphene.

monolayer graphene that we have measured to be ~18% and 7 wt%, respectively. This suggests the possibility of full sediment recycling and the eventual increase of the yield towards 7−12 wt% (relative to the starting graphite mass).

IDENTIFICATION OF MONOLAYERS BY ELECTRON DIFFRACTION

A more definitive identification of graphene can be made by analysis of electron diffraction patterns[45]. As an example of this, Fig. 3a,b shows what appear to be a graphene monolayer and a graphene bilayer, respectively. Figure 3b is particularly interesting as the right side of the flake consists of at least two layers, whereas on the left side, a single monolayer protrudes. Figure 3c shows the normal-incidence electron diffraction pattern of the flake in Fig. 3a. This pattern shows the typical sixfold symmetry expected for graphite/graphene[44,45], allowing us to label the peaks with the Miller−Bravais (*hkil*) indices. Figure 3d,e shows normal-incidence selected-area diffraction patterns for the flake in Fig. 3b, taken with beam positions close to the black and white dots, respectively. This means we expect one pattern (Fig. 3d) to reflect monolayer graphene and the other (Fig. 3e) to reflect multilayer graphene. In both cases we see a hexagonal pattern similar to that in Fig. 3c. The main difference between Fig. 3d and Fig. 3e is that for the multilayers (Fig. 3e), the {2110} spots appear to be more intense relative to the {1100} spots. This is an important observation, as for multilayers with Bernal (AB) stacking, computational studies have shown that the intensity ratio is $I_{\{1100\}}/I_{\{2110\}} < 1$, whereas for monolayers it is $I_{\{1100\}}/I_{\{2110\}} > 1$ (ref. 46). Virtually all the objects identified in all the images as multilayers displayed a ratio of $I_{\{1100\}}/I_{\{2110\}} < 1$, demonstrating that AB stacking is predominant in these samples[46].

This identification of AB stacking in these thin multilayers allows us to differentiate monolayer from multilayer graphene by inspection of the intensity ratio $I_{\{1100\}}/I_{\{2110\}}$. To do this, we

plot a line section through the (1−210)−(0−110)−(−1010)−(−2110) axis for the patterns in Fig. 3c−e in Fig. 3f−h. In Fig. 3f,g we see that the inner peaks, (0−110) and (−1010), are more intense than the outer ones, (1−210) and (−2110), confirming that that both the flake in Fig. 3a and the region marked by the black dot in Fig. 3b are monolayers. Conversely, Fig. 3h shows inner peaks that are less intense than the outer ones, confirming that the area around the white dot in Fig. 3b consists of more than one layer. Further confirmation of the presence of monolayer graphene can be found by measuring the diffraction peak intensity as a function of tilt angle (see Supplementary Information, Section S2.8).

We can use the fact that the ratio of the intensity of the {1100} to the {2110} peaks gives an unambiguous local identification of monolayer versus multilayer to provide information on the yield of monolayer graphene. We measured the diffraction pattern of 45 flakes before measuring the intensity ratio $I_{\{1100\}}/I_{\{2110\}}$. These ratios are plotted as a histogram in Fig. 3i. We get a bimodal distribution, with peaks centred at $I_{\{1100\}}/I_{\{2110\}} = 0.35$ and $I_{\{1100\}}/I_{\{2110\}} = 1.5$, representing multilayer and monolayer graphene, respectively. These results agree well with reported experimental intensity ratios of $I_{\{1100\}}/I_{\{2110\}} \approx 0.4$ for bilayer graphene and $I_{\{1100\}}/I_{\{2110\}} \approx 1.4$ for monolayer graphene[45]. Although these data suggest a yield of 51% monolayer graphene, this is certainly an overestimate, as selected-area electron diffraction can give monolayer-like patterns for multilayers, such as that in Fig. 3b, when the beam is incident on a protruding monolayer. Better statistics can be found by counting the number of layers per flake, as shown in Fig. 2h. However, we can use electron diffraction to check the accuracy of our image analysis, showing that we can reproducibly use it to identify monolayer graphene, thus confirming the results presented in Fig. 2h. The presence of monolayers was also confirmed by measuring TEM identified layers by Raman spectroscopy (see Supplementary Information, Section S2.9).
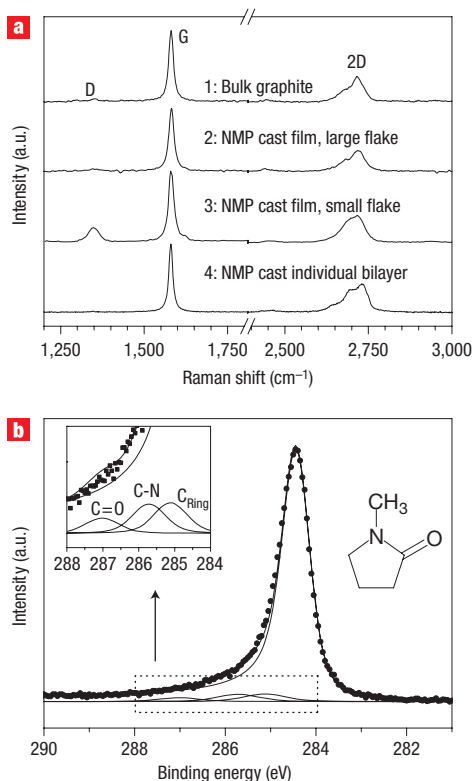
Figure 4 Evidence for defect-free graphene. a, Raman spectra for bulk graphite (1), a vacuum filtered film with the laser spot focused on a large ($\sim$5 µm) flake (2), a vacuum filtered film with the laser spot focused on a small ($\sim$1 µm) flake (3), a large ($\sim$10 µm) bilayer (4). Note that for spectra 2 and 4, the D line is absent, indicating that virtually no defects are present. For the small flake (spectrum 3), a weak D line is apparent, consistent with edge effects[47]. **b**, A carbon 1s core-level XPS spectrum for a thin film ($\sim$30 nm), vacuum-deposited from a graphene dispersion and dried in a vacuum oven at room temperature. The Shirley background has been subtracted for clarity. Main fit line represents graphitic carbon (C−C). The remainder, $\sim$286 eV, can be very well fitted considering only residual NMP without the need for any oxide lines. The smaller fit lines represent residual NMP; C$_{ring}$, carbon in the NMP ring bonded to two hydrogen atoms; C−N, carbon in the NMP molecule bonded to a nitrogen atom; C = O, carbon in the NMP ring double bonded to an oxygen atom. Left inset: enlarged view of the NMP fit lines (combined and individual). Right inset: structure of NMP.

EVIDENCE FOR DEFECT-FREE GRAPHENE

Although Fig. 1d suggests a van der Waals type solvent−graphene interaction, it is crucial to definitively rule out any inadvertent basal-plane functionalization, which could alter the electronic structure. Figure 4a shows Raman spectra of three different flakes with the spectrum of bulk graphite for comparison (see Supplementary Information, Section S1.4). Spectra 2 and 3 were measured on thin films prepared by vacuum filtration onto alumina filters by focusing the spot on a large diameter ($\sim$5 µm) and a small diameter ($\sim$1 µm) flake, respectively. Spectrum 4 was measured on a significantly large bilayer (>10 µm) (see Supplementary Information, Sections S1.1 and S2.9). The G line ($\sim$1,580 cm^{-1}) and 2D line ($\sim$2,700 cm^{-1}) are clearly visible in all cases. However, the D peak ($\sim$1,350 cm^{-1}) is only visible in the spectrum of the very small flake, as expected due to edge effects[47]. These data, in particular the spectrum for the individual bilayer, demonstrate that our process does not introduce significant structural defects[47], such as epoxides covalently bonded to the basal plane[22]. In addition, we recorded Raman spectra for individual flakes deposited on marked TEM grids, allowing us to identify monolayers, bilayers and multilayers from both the TEM image and the shape of the 2D band, confirming the quality of our exfoliation (see Supplementary Information, Section S2.9). Furthermore, X-ray photoelectron spectroscopy, as shown in Fig. 4b (see Supplementary Information, Section S3.2) and infrared spectroscopy (see Supplementary Information, Section S3.3) show the absence of oxidization typically associated with GO (refs 18,19). These experiments again confirm that we can produce high-quality, unoxidized graphite and graphene flakes in solution.

FURTHER CHARACTERIZATION OF LIQUID-PHASE EXFOLIATION

We can briefly illustrate the potential of this method of graphite exfoliation by using it to make thin graphene films. Raman and SEM analyses show that these films consist predominately of thin graphite flakes with fewer than five layers (see Supplementary Information, Section S1.4). X-ray photoelectron spectroscopy measurements show that these films have $\sim$11 wt% residual NMP after drying at room temperature at $\sim$1 × 10^{-3} mbar. This value remained unchanged after a subsequent vacuum anneal at 400 °C (see Supplementary Information, Section S3.2). Combustion analysis gave an NMP content of $\sim$10 wt% after room-temperature drying ($\sim$1 × 10^{-3} mbar), which can be reduced to <7 wt% after annealing (see Supplementary Information, Section S3.4). These films have conductivities of $\sim$6,500 S m^{-1}, similar to reduced graphene oxide films[19], and optical transparencies of $\sim$42% (see Supplementary Information, Section S4.0).

We also demonstrate polystyrene−graphene composites at high volume fraction. We measured the conductivity of such composites to be $\sim$100 S m^{-1} (see Supplementary Information, Section S5.0) for 60−80 vol% films, comparable to the most conductive polymer−nanotube composites[48] and significantly higher than those quoted for graphene-oxide-based composites[20]. Finally, we deposited graphene monolayers and multilayers on SiO$_2$ surfaces by means of spray coating, demonstrating that this processing method can potentially be used to prepare samples for microelectronic applications (see Supplementary Information, Section S2.7).

CONCLUSION

We have demonstrated a scalable method to produce high-quality, unoxidized graphite and graphene flakes from powdered graphite. By using certain solvents, graphene can be dispersed at concentrations of up to 0.01 mg ml^{-1}. These dispersions can then be used to deposit flakes by spray coating, vacuum filtration or drop casting. By adding polymers they can be turned into polymer−composite dispersions. We believe that this work opens up a whole new vista of potential applications from sensor or devices to transparent electrodes and conductive composites.

References
1. Geim, A. K. & Novoselov, K. S. The rise of graphene. *Nature Mater.* **6**, 183–191 (2007).
2. Novoselov, K. S. *et al.* Two-dimensional gas of massless Dirac fermions in graphene. *Nature* **438**, 197–200 (2005).
3. Novoselov, K. S. *et al.* Electric field effect in atomically thin carbon films. *Science* **306**, 666–669 (2004).
4. Zhang, Y. B., Tan, Y. W., Stormer, H. L. & Kim, P. Experimental observation of the quantum Hall effect and Berry's phase in graphene. *Nature* **438**, 201–204 (2005).
5. Pisana, S. *et al.* Breakdown of the adiabatic Born−Oppenheimer approximation in graphene. *Nature Mater.* **6**, 198–201 (2007).
6. Blake, P. *et al.* Graphene-based liquid crystal device. *Nano Lett.* **8**, 1704–1708 (2008).
7. Novoselov, K. S. *et al.* Two-dimensional atomic crystals. *Proc. Natl Acad. Sci. USA* **102**, 10451–10453 (2005).

ARTICLES

8. Bolotin, K. I. *et al*. Ultrahigh electron mobility in suspended graphene. *Solid State Commun.* **146**, 351–355 (2008).
9. Morozov, S. V. *et al*. Giant intrinsic carrier mobilities in graphene and its bilayer. *Phys. Rev. Lett.* **1**, 016602 (2008).
10. Du, X., Skachko, I., Barker, A. & Andrei, E. Y. Approaching ballistic transport in suspended graphene. *Nature Nanotech.* **3**, 491–495 (2008).
11. Berger, C. *et al*. Electronic confinement and coherence in patterned epitaxial graphene. *Science* **312**, 1191–1196 (2006).
12. Ohta, T. *et al*. Morphology of graphene thin film growth on SiC(0001). *New J. Phys.* 023034 (2008).
13. Zhou, S. Y. *et al*. Origin of the energy bandgap in epitaxial graphene—Reply. *Nature Mater.* **7**, 259–260 (2008).
14. Marchini, S., Gunther, S. & Wintterlin, J. Scanning tunnelling microscopy of graphene on Ru(0001). *Phys. Rev. B* **76**, 075429 (2007).
15. de Parga, A. L. V. *et al*. Periodically rippled graphene: Growth and spatially resolved electronic structure. *Phys. Rev. Lett.* **1**, 056807 (2008).
16. Sutter, P. W., Flege, J.–I. & Sutter, E. A. Epitaxial graphene on ruthenium. *Nature Mater.* **7**, 406–411 (2008).
17. Pan, Y. *et al*. Millimetre-scale, highly ordered single crystalline graphene grown on Ru (0001) surface. ArXiv:0709.2858 (2008).
18. Eda, G., Fanchini, G. & Chhowalla, M. Large-area ultrathin films of reduced graphene oxide as a transparent and flexible electronic material. *Nature Nanotech.* **3**, 270–274 (2008).
19. Li, D. *et al*. Processable aqueous dispersions of graphene nanosheets. *Nature Nanotech.* **3**, 101–105 (2008).
20. Stankovich, S. *et al*. Graphene-based composite materials. *Nature* **442**, 282–286 (2006).
21. Wang, X., Zhi, L. J. & Mullen, K. Transparent, conductive graphene electrodes for dye-sensitized solar cells. *Nano Lett.* **8**, 323–327 (2008).
22. Stankovich, S. *et al*. Synthesis of graphene-based nanosheets via chemical reduction of exfoliated graphite oxide. *Carbon* **45**, 1558–1565 (2007).
23. Jung, I. *et al*. Simple approach for high-contrast optical imaging and characterization of graphene-based sheets. *Nano Lett.* **7**, 3569–3575 (2007).
24. Dresselhaus, M. S. & Dresselhaus, G. Intercalation compounds of graphite. *Adv. Phys.* **30**, 139–326 (1981).
25. Viculis, L. M., Mack, J. J. & Kaner, R. B. A chemical route to carbon nanoscrolls *Science* **299**, 1361–1361 (2003).
26. Chen, G. H. *et al*. Preparation and characterization of graphite nanosheets from ultrasonic powdering technique. *Carbon* **42**, 753–759 (2004).
27. Li, X. L. *et al*. Chemically derived, ultrasmooth graphene nanoribbon semiconductors. *Science* **319**, 1229–1232 (2008).
28. Niyogi, S. *et al*. Solution properties of graphite and graphene. *J. Am. Chem. Soc.* **128**, 7720–7721 (2006).
29. Furtado, C. A. *et al*. Debundling and dissolution of single-walled carbon nanotubes in amide solvents. *J. Am. Chem. Soc.* **126**, 6095–6105 (2004).
30. Giordani, S. *et al*. Debundling of single-walled nanotubes by dilution: observation of large populations of individual nanotubes in amide solvent dispersions. *J. Phys. Chem. B* **110**, 15708–15718 (2006).
31. Landi, B. J., Ruf, H. J., Worman, J. J. & Raffaelle, R. P. Effects of alkyl amide solvents on the dispersion of single-wall carbon nanotubes. *J. Phys. Chem. B* **108**, 17089–17095 (2004).
32. Hasan, T. *et al*. Stabilization and 'Debundling' of single-wall carbon nanotube dispersions in N-methyl-2-pyrrolidone (NMP) by polyvinylpyrrolidone (PVP). *J. Phys. Chem. C* **111**, 12594–12602 (2007).
33. Bergin, S. D. *et al*. Exfoliation in ecstasy: liquid crystal formation and concentration-dependent debundling observed for single-wall nanotubes dispersed in the liquid drug γ-butyrolactone. *Nanotechnology* **18**, 455705 (2007).
34. Bergin, S. D. *et al*. Towards solutions of SWNT in common solvents. *Adv. Mater.* **20**, 1876–1881 (2007).
35. Abergel, D. S. L. & Fal'ko, V. I. Optical and magneto-optical far-infrared properties of bi-layer graphene. *Phys. Rev. B* **75**, 155430 (2007).
36. Hildebrand, J. H., Prausnitz, J. M. & Scott, R. L. Regular and related solutions 1st edn (Van Nostrand Reinhold Company, New York, 1970).
37. Lyklema, J. The surface tension of pure liquids—thermodynamic components and corresponding states. *Coll. Surf. A* **156**, 413–421 (1999).
38. Tsierkezos, N. G. & Filippou, A. C. Thermodynamic investigation of N,N-dimethylformamide/toluene binary mixtures in the temperature range from 278.15 to 293.15 K. *J. Chem. Therm.* **38**, 952–961 (2006).
39. Benedict, L. X. *et al*. Microscopic determination of the interlayer binding energy in graphite. *Chem. Phys. Lett.* **286**, 490–496 (1998).
40. Girifalco, L. A. & Good, R. J. A theory for the estimation of surface and interfacial energies. 1. Derivation and application to interfacial tension. *J. Phys. Chem.* **61**, 904–909 (1957).
41. Hodak, M. & Girifalco, L. A. Fullerenes inside carbon nanotubes and multi-walled carbon nanotubes: optimum and maximum sizes. *Chem. Phys. Lett.* **350**, 405–411 (2001).
42. Zacharia, R., Ulbricht, H. & Hertel, T. Interlayer cohesive energy of graphite from thermal desorption of polyaromatic hydrocarbons. *Phys. Rev. B* **69**, 155406 (2004).
43. Jeong, S. H. *et al*. Preparation of aligned carbon nanotubes with prescribed dimensions: Template synthesis and sonication cutting approach. *Chem. Mater.* **14**, 1859–1862 (2002).
44. Meyer, J. C. *et al*. The structure of suspended graphene sheets. *Nature* **446**, 60–63 (2007).
45. Meyer, J. C. *et al*. On the roughness of single- and bi-layer graphene membranes. *Solid State Commun.* **143**, 101–109 (2007).
46. Horiuchi, S. *et al*. Carbon nanofilm with a new structure and property. *Jpn J. Appl. Phys. Lett.* **42**, L1073–L1076 (2003).
47. Ferrari, A. C. *et al*. Raman spectrum of graphene and graphene layers. *Phys. Rev. Lett.* **97**, 187401 (2006).
48. Blighe, F. M., Hernandez, Y., Blau, W. J. & Coleman, J. N. Observation of percolation-like scaling, far from the percolation threshold, in high volume fraction, high conductivity polymer–nanotube composite films. *Adv. Mater.* **19**, 4443–4447 (2007).

Author contributions
J.N.C. conceived and designed the experiments. Y.H., V.N., M.L., F.M.B., Z.S., S.D., B.H., M.B., P.N., S.K., R.G. and V.S. performed the experiments. I.T.McG., R.G., A.C.F. and J.N.C. analysed the data. Y.K.G., J.J.B., G.D., R.G., J.H., A.C.F. and J.N.C. contributed materials/analysis tools. A.C.F. and J.N.C. co-wrote the paper. Y.H. and V.N. contributed equally to this work. All authors discussed the results and commented on the manuscript.